Syringomyelia Hydrodynamics: An In Vitro Study Based on In Vivo Measurements

Bryn A. Martin
Wojciech Kalata
Francis Loth
Thomas J. Royston

University of Illinois at Chicago,
Department of Mechanical and Industrial Engineering,
Chicago, IL

John N. Oshinski
Emory University,
Department of Radiology and Biomedical Engineering,
Atlanta, GA

A simplified in vitro model of the spinal canal, based on in vivo magnetic resonance imaging, was used to examine the hydrodynamics of the human spinal cord and subarachnoid space with syringomyelia. In vivo magnetic resonance imaging (MRI) measurements of subarachnoid (SAS) geometry and cerebrospinal fluid velocity were acquired in a patient with syringomyelia and used to aid in the in vitro model design and experiment. The in vitro model contained a fluid-filled coaxial elastic tube to represent a syrinx. A computer controlled pulsatile pump was used to subject the in vitro model to a CSF flow waveform representative of that measured in vivo. Fluid velocity was measured at three axial locations within the in vitro model using the same MRI scanner as the patient study. Pressure and syrinx wall motion measurements were conducted external to the MR scanner using the same model and flow input. Transducers measured unsteady pressure both in the SAS and intra-syrinx at four axial locations in the model. A laser Doppler vibrometer recorded the syrinx wall motion at 18 axial locations and three polar positions. Results indicated that the peak-to-peak amplitude of the SAS flow waveform in vivo was approximately tenfold that of the syrinx and in phase ($SAS \sim 5.2 \pm 0.6$ *ml/s*, $syrinx \sim 0.5 \pm 0.3$ *ml/s*). *The in vitro flow waveform approximated the in vivo peak-to-peak magnitude* ($SAS \sim 4.6 \pm 0.2$ *ml/s*, $syrinx \sim 0.4 \pm 0.3$ *ml/s*). *Peak-to-peak in vitro pressure variation in both the SAS and syrinx was approximately 6 mm Hg. Syrinx pressure waveform lead the SAS pressure waveform by approximately 40 ms. Syrinx pressure was found to be less than the SAS for* $\sim$200 *ms during the 860-ms flow cycle. Unsteady pulse wave velocity in the syrinx was computed to be a maximum of* $\sim$25 *m/s. LDV measurements indicated that spinal cord wall motion was nonaxisymmetric with a maximum displacement of* $\sim$140 μ*m, which is below the resolution limit of MRI. Agreement between in vivo and in vitro MR measurements demonstrates that the hydrodynamics in the fluid filled coaxial elastic tube system are similar to those present in a single patient with syringomyelia. The presented in vitro study of spinal cord wall motion, and complex unsteady pressure and flow environment within the syrinx and SAS, provides insight into the complex biomechanical forces present in syringomyelia.* [DOI: 10.1115/1.2073687]

Introduction

The brain and spinal cord are surrounded by cerebrospinal fluid (CSF). CSF moves in a pulsatile manner through the complicated subarachnoid (SAS), spinal canal, and ventricular spaces of the brain [1]. CSF is produced at an average rate of 0.3–0.7 ml/min in the ventricular cavity and primarily removed through the superior sagittal sinus [2]. It is a clear fluid having viscosity nearly that of water and, in a healthy person, is composed of dilute amounts of proteins and monoamines. The fluid is utilized to supply nutrients and remove waste from the brain. The average healthy adult has approximately 125 ml of CSF [3], with the majority residing in the cranial cavity.

CSF flow is passive and the pulsatile nature of CSF flow has been associated with changes in blood volume within the cranial cavity due to the cardiac cycle [3]. This blood volume change is a result of phase difference between blood influx and outflow to and from the brain. Since the cranium acts as a rigid volume, the CSF pulses with each cardiac cycle, through the SAS and around the spinal cord. Each cardiac cycle has equal amounts of fluid motion in both systole and diastole with no net flow [4]. Blood volume changes in the brain due to the cardiac cycle may not be the only cause of CSF motion. In an experiment by Dunbar et al. [5], CSF motion in the spinal canal was still found in dogs with their cervical canal blocked. It is also known that changes in posture result in movement of the spinal cord position relative to the vertebrae, resulting in variation in CSF flow [2]. A relationship between CSF pressure and changes in intrathorax pressure has also been shown [6].

CSF also serves to provide damping between the brain and skull when sudden movements of the cranium occur. Various pathological conditions can be caused by or associated with the obstruction of CSF flow. These include Chiari malformation (Fig. 1), syringomyelia, and hydrocephalus. The following study examines the hydrodynamic conditions that are present in syringomyelia (Fig. 2). This pathology is characterized by the formation of a fluid filled cyst (or syrinx) in the spinal cord. The fluid in the syrinx has been shown to have similar properties as CSF in the SAS and therefore has been thought to penetrate through the spinal cord from the SAS [7]. The formation of the fluid filled syrinx has been associated with CSF flow obstruction in the SAS of the brain and spinal canal. However, the formation of a syrinx is not always present when CSF flow is obstructed. One type of CSF flow obstruction that can occur is caused by the Chiari I malformation, which is characterized by a reduction in size of the posterior fossa and elongation or displacement of the cerebellar tonsils through the foramen magnum into the upper spinal canal (Fig. 1).

Due to the complex nature of CSF flow and SAS geometry, it has been challenging to determine the internal forces associated with the obstruction of CSF flow as it relates to pathology. Recent

Contributed by the Bioengineering Division for publication in the JOURNAL OF BIOMECHANICAL ENGINEERING. Manuscript received January 26, 2005; final manuscript received July 18, 2005. Review conducted by Michael Sacks.

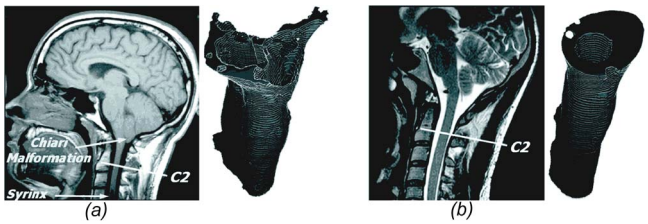

Fig. 1 Sagittal MRI of head and 3D reconstruction of subcranial subarachnoid space. (*a*) Patient with Chiari malformation and syringomyelia (T1 image). (*b*) Healthy subject (T2 image).

interest has been focused on the examination of hydrodynamic conditions of the CSF in the SAS that may play a role in the pathogenesis of syringomyelia. Research primarily falls under one of two categories, the first being computational fluid dynamic simulation or fluid structure interaction, and the other being theory based on clinical observation. These studies have broadened understanding of the elusive origins of syringomyelia.

Considerable study has been directed towards determination and analysis of CSF flow velocities through the spinal cavity using dynamic phase contrast MRI (pcMR) [1,8]. However, few studies have been empirically validated by direct comparison to the actual mechanical forces that occur during pulsation of CSF within the SAS. This is primarily due to the fact that acquiring in vivo measurements of pressure is an invasive procedure that presents risk to the patient. The goal of the present study is to validate and test a phantom flow model that mimics the hydrodynamics present in a patient with syringomyelia in order to better quantify the biomechanical environment. A better understanding of these biomechanical forces may elucidate the importance of hydrodynamics in the progression of syringomyelia.

Overview of Syringomyelia Theories

A wide variety of theories have been proposed over the last two centuries to explain the development and progression of syringomyelia. The majority of recent theories attribute formation of the syrinx to pathological craniospinal hydrodynamics caused by the obstruction of CSF flow. An in-depth historical review of the pathophysiology of syringomyelia was detailed by Klekamp in 2002 [9]. In 1959, Gardner proposed that syringomyelia originated from a hydrodynamic mechanism [10]. In 1969, Williams proposed a "suck and slosh" theory in which a craniospinal pressure dissociation occurs due to the ball-valve effect at the foramen magnum [11,12]. This theory asserts that CSF is allowed to flow cranially but not caudally during valsalva, thereby forcing CSF into the spinal cord. Ball and Dayan proposed in 1972 that CSF is forced though the Virchow-Robin spaces into the spinal cord forming a cyst [13].

In 1994, Oldfield et al. developed a systolic pressure theory for the development of a syrinx [14]. This theory proposes that the brain expands during systole causing a pressure wave to travel down the spinal cord SAS. If the pressure wave is obstructed at the foramen magnum, the cerebellar tonsils are forced to distend, causing a pressure wave to move the spinal cord downward. This results in the enlargement of the syrinx by forcing CSF through the perivascular and interstitial spaces. In 1999, Greitz et al. proposed that the syrinx develops as a result of a differential pressure propagation mechanism where the normal CSF pressure wave is obstructed in the SAS and instead transmitted down the spinal cord [15,16]. Greitz explained that the syrinx is first caused by mechanical pulling of the spinal cord through a number of proposed means, after which the cord is filled with extracellular fluid that slowly circulates through the spinal cord.

The hydrodynamic origin of syringomyelia has been examined through mathematical analysis of a fluid-filled co-axial elastic tube system by Carpenter et al. and Berkouk et al. [12,17]. Vibration of fluid-filled thin coaxial tubelike structures has been examined in a number of areas [18–22]. Carpenter's work is based on classical theory of wave propagation in elastic tubes. This theory assumes axisymmetric quasi-one-dimensional wave propagation and flexion of the elastic tubes. The movement of the tubes is shown to be largely dependant on the ratio of the cross-sectional area of the tubes. In vivo syrinx wall movement has been observed intraoperatively through use of ultrasound by Heiss et al. [23].

The theories detailed give a better understanding of the pathogenesis of syringomyelia. However, Carpenter explains that, "The overriding problem with these theories is, at best, they only explain the origins of communicating syringomyelia, whereas the great majority of cases are noncommunicating" [12]. Furthermore, Carpenter asserts that the empirical evidence used to explain the origin of noncommunicating syringomyelia detailed by Heiss [23] and Oldfield [14], "… is difficult to reconcile in its entirety with the principles of mechanics" [12]. Klekamp has reported similar lack of explanation in current theories stating that, "Various ideas and hypotheses have been brought forward to explain the development of syringomyelia in the past two centuries. None of them offers a sufficient basis to serve as a concept for the treatment of all affected patients" [9]. In 2004, Levine stated that, "These theories are implausible biophysically because none postulates a pump adequate to drive fluid through these (perivascular) spaces. None of the theories can explain why syrinx pressure is higher than CSF pressure; why extensive gliosis, edema, and vascular wall thickening regularly occur; and why the composition of syrinx fluid is not identical with that of CSF" [24].

Considering the analysis of syringomyelia theories by the cited researchers and others, it can be concluded that uncertainty exists due to mechanical intuition and lack of evidence. Complete mechanical explanation and observation for the pooling of CSF in the syrinx has not been detailed. Therefore, the current hydrodynamic theories of syringomyelia may benefit from the detailed measurement of unsteady pressure and flow in the SAS and syrinx as well as the wall motion of the syrinx. These measurements require significant risk to the patient and therefore are not likely to be conducted. In vitro flow models have been used extensively for both validation of numerical simulations and to acquire otherwise difficult to obtain in vivo measurements [25,26]. Thus, a physical flow model of the spinal canal that closely represents the in vivo hydrodynamics of syringomyelia may serve well to gain a better understanding of the system hydrodynamics as well as pathogenesis of syringomyelia. This paper describes a series of experiments using such a physical flow model. MRI measurements were

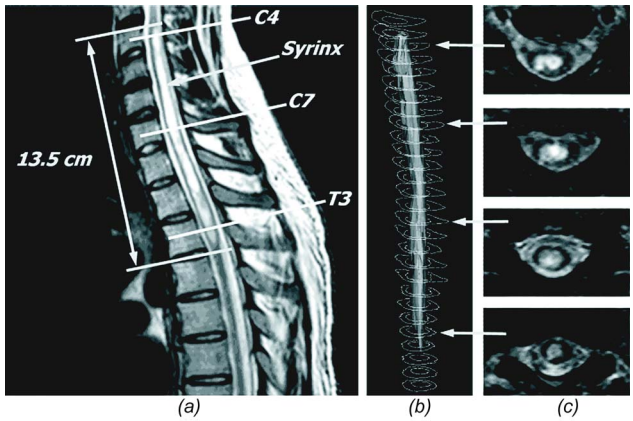

Fig. 2 MRI of a patient with Chiari malformation and syringomyelia. (*a*) Patient's lower cervical and thoracic region with syringomyelia. (*b*) 3D view of syrinx with contours, indicating the SAS reconstructed from axial images. (*c*) MRI images of the spinal canal and syrinx at various axial locations.

conducted using the flow model in the same scanner in which in vivo measurements were obtained on a patient with syringomyelia in order to assess how well the in vitro model mimics the in vivo case. Bench-top studies were then conducted to measure unsteady pressure within the SAS and syrinx as well as syrinx wall motion.

Methods

Patient History. The patient for the *in vivo* MRI study was a 30-year-old male diagnosed with Chiari I malformation reporting symptoms of middle and upper back pain, right arm numbness, and headaches. The patient provided informed consent and the study was approved by the University's Institutional Review Board (IRB).

In Vivo MRI Measurements. Images used for the in vitro model design parameters were based on MRI scans from a 1.5-T Philips Gyroscan NT Intera MRI scanner (Philips Medical Systems, Best, The Netherlands). Both anatomy and cine flow images were acquired. The MRI anatomy scans included sets of images in sagittal and axial planes in the head and in the cervical and thoracic spine. A set of high-resolution, steady-state free procession (SSFP) axial images of the lower brain and upper cervical region were acquired and used to define the Chiari I malformation in detail. A set of fast, segmented, T2-weighted spin-echo axial images defined the region of syringomyelia in the lower cervical and thoracic regions. These sets of axial images were processed by MIMICS (Materialise, Ann Arbor, MI) to obtain three-dimensional (3D) models of the SAS and syrinx, which are shown in Fig. 1. Phase contrast MRI flow measurements were obtained from the patient at the second, fourth, and seventh cervical vertebrae levels (C2, C4, C7) as well as the third thoracic vertebrae level (T3) as shown in Fig. 2. Syrinx flow was measured at levels C7 and T3 as indicated in Fig. 2. High-resolution balanced-steady-state free procession cine (bSSFP) images gated to the cardiac cycle were acquired at C2 and C4. These cine loops acquired 32 frames over the cardiac cycle and were used to investigate changes in spinal cord and syrinx area during the cardiac cycle.

Flow waveforms were obtained from the recorded velocity for each pixel from pcMR images. Pixel velocity was integrated for an area of interest to obtain flow using image processing software developed within MATLAB (Mathworks 12.0, Natick, MA). The process involved integration of the velocity over a manually selected cross-sectional region for an entire cardiac cycle as detailed by Kalata [27]. The basic equation for this process is given by $Q(t)=\Sigma A_{\text{pixel}}[V_{\text{pixel}}(t)]$, where A_{pixel} is the area of one MRI pixel, V_{pixel} is the velocity for the corresponding pixel, and $Q(t)$ is the summation of the flow for each pixel of interest.

Reynolds (Re) and Womersley (α) numbers were computed based on peak flow rate (Q_{peak}) and hydraulic diameter (D_h). ($\text{Re}=4Q_{\text{peak}}/(\upsilon P_{\text{wet}})$, $D_h=4A_{\text{cs}}/P_{\text{wet}}$, and $\alpha=(2A_{\text{cs}}/P_{\text{wet}})\sqrt{\omega/\upsilon}$ where A_{cs} is cross-sectional area, P_{wet} is wetted perimeter, υ is kinematic viscosity, ω is angular velocity). A_{cs} and P_{wet} were based on 3D models obtained from MIMICS. These models were exported in StrataSys Layer (SSL) format. Additionally, they were smoothed using in-house developed software as detailed by Yedavalli et al. [28]. A_{cs} and P_{wet} computations of SAS and syrinx for both in vivo and in vitro cases were performed in MATLAB [27].

The volume change of a given section of the syrinx as a function of time was determined as follows. This technique enables quantification of the cross-sectional area change of the spinal cord even in cases when it is below the in plane pixel resolution of MRI through the measurement of the flow waveform into and out of a control volume. In the case of the spinal cord model, this control volume is defined by two parallel planes that are each orthogonal to CSF flow separated by a finite distance (L). For the in vivo calculation, plane separation was 6 cm. A volume that accommodates the changes of flow waveforms between two different axial locations was obtained. It was computed using trapezoidal rule by initially computing volume changes for each time increment (calculation of area under the curve of the flow difference into and out-of the region of interest). Then in order to obtain volume at specific time interval, the volume changes from the first to current time intervals were added ($\text{Vol}_i=\Sigma_{i=1}^{n}[dQ_{i-1}+dQ_i][t_i-t_{i-1}]/2$). At the end, volume throughout the cardiac cycle [Vol(t)] was normalized with the temporal mean value. The change in average cross-sectional area as a function of time [$\Delta A(t)$] was obtained since it is related to volume by $\Delta A(t)=\Delta\text{Vol}(t)/L$.

In Vitro Model Spinal Cord. While the mechanical properties of a healthy human spinal cord have not, to our knowledge, been reported in the literature, some information is available detailing animal spinal cord properties. The approximate Young's modulus for bovine and guinea pig spinal cord are 200–3400 and 600–2000 kPa, respectively [29–31]. The syrinx portion of the in vitro model was constructed in order to have a Young's modulus similar to these values. Note that this is significantly more rigid than the Young's modulus for blood vessels (arterial and venous tissue are 100–250 and 150–400 kPa, respectively) [32]. The syrinx portion of the phantom model was constructed using a plastic polymer (Sylgard 184, G.E. Plastics, Pittsfield, MA). The mechanical properties were altered by varying the ratio of curing agent from the factory specified 10:1 ratio. This technique has been examined in the literature [33], and tested experimentally in house. A 30:1 ratio produced a material with a Young's modulus of 175 kPa as measured experimentally by a weight and elongation. This mixing ratio was used for the syrinx portion of the model in order to approximately match spinal cord elasticity. It is important to note the possibility that the spinal cord and surrounding tissues in patients with syringomyelia may have different mechanical properties than those without this disease.

The syrinx geometry was simplified as a constant radius coaxial tube with dimensions chosen to approximate a patient with syringomyelia (Fig. 2). The spinal cord outer diameter was 1.90 cm with an inner syrinx diameter of 1.52 cm, total length of 18 cm, and approximate density of 1046 kg/m^3. The syrinx geometry was constructed by casting Sylgard around a copper pipe with heat shrink tubing as the exterior confinement. Model cross-sectional geometry was nearly constant over the entire length. However, the model was not axisymmetric due to unintended variations in wall thickness during model curing. Variation in wall thickness is quantified in the results section. The tubular model was carefully removed with soapy water after one week of curing time at room temperature.

In Vitro Model SAS. SAS construction consisted of casting Sylgard at a 10:1 ratio in a plastic box around a 2.54-cm-diameter aluminum pipe. The model was left to cure for one week at room temperature. Sylgard at 10:1 ratio was tested and determined to have a Young's modulus of approximately 1.45 GPa. Four pressure ports were cast in to the model in order to measure pressure along the SAS. The remainder of the model was constructed using PVC piping with screws fitted on the ends in order to fasten and tension the syrinx in place.

One important feature of the model is the cross-sectional area of the internal syrinx catheter and the vertical external PVC piping (Fig. 3). Since the volume change during each flow cycle is fixed, these areas dictate the pressure head forcing on the SAS and syrinx cavity. The pressure head is dependant on the fluid column height change during each flow cycle. Thus, by changing the size and ratio of these areas, backpressure on the SAS and syrinx cavity can be varied independently. The exit pipe diameter was selected to provide a pressure variation of ~6 mm Hg, which is similar in magnitude to that observed in vivo [23].

In Vitro Model Assembly. The syrinx and subarachnoid space were assembled in such a way as to minimize tension on the

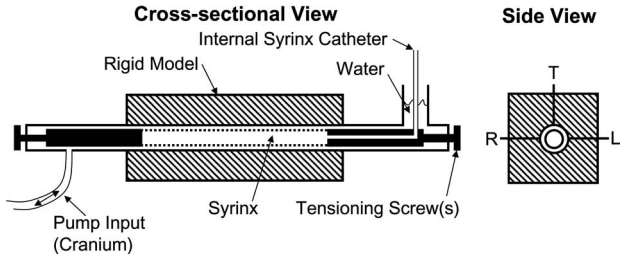

Fig. 3 In vitro phantom CSF system model, cross-sectional and side view. The internal syrinx catheter (depicted) is clamped to alter the boundary condition from "open to atmospheric pressure" to "closed to atmospheric pressure."

syrinx region. This was achieved by relaxing the tension screws in such a way so as to support its own weight without touching the SAS portion of the model. The tension on the syrinx caused a total strain of approximately 1 mm (~0.5%) as estimated from a measurement of the tubes elongation while assembled. The syrinx region was filled with water through the hollow internal syrinx catheter as depicted in Fig. 3. This port also served to alter the boundary condition of the syrinx from open or closed to atmospheric pressure by clamping the internal syrinx catheter shut. The effect of changing the boundary condition from closed to open is an important feature of the model and is examined in the discussion section.

Pulsatile Pump and Flow Input. A computer controlled pulsatile syringe pump was constructed to be capable of producing flow waveforms similar to those measured in vivo (~1 cc/s pulsation) and connected to the model as shown in Fig. 4. Note, the pump delivers pulsatile flow to the SAS only (SAS diameter 2.54 cm). The syrinx is sealed within the model and vented through the external syrinx catheter (open condition only), which is representative of a noncommunicating syrinx. In addition, the syrinx is only compliant between the rigid tensioning screws (dotted lines in Fig. 3). The pulsatile pump consisted of a tubular linear servo motor (TT Micro Model #TB1106, Copley Controls Corp., Canton, MA) that forced a precision syringe in a pulsatile manner according to a voltage signal generated by a laptop computer. Spline interpolation of the MRI derived flow waveform from the

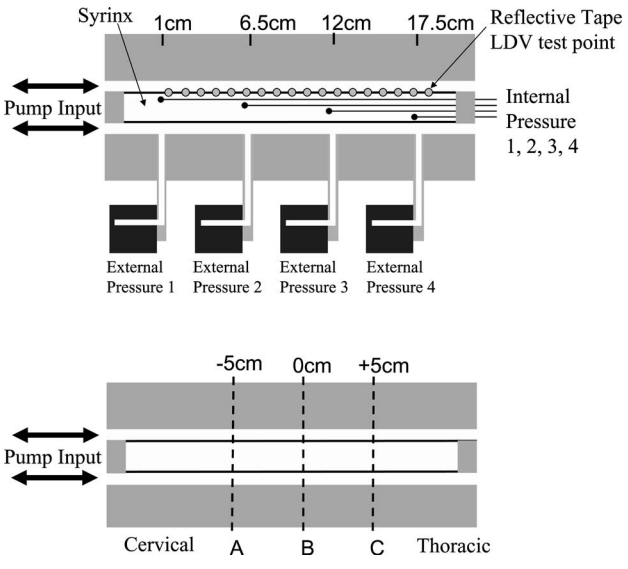

Fig. 4 Experimental configuration for the pressure and spinal cord wall motion experiment (top) and MRI experiment (bottom)

C2 region was used to generate the continuous voltage signal. The motor was equipped with a linear encoder (RG24 Digital Read Model #RGH24X30A00A, Renishaw, Hoffman Estates, IL) to track position of the syringe to 1 μm. Ten-poise spindle oil was used to lubricate the syringe shaft during operation. An oil water boundary separated the syringe from the water that entered the flow model through use of a graduated cylinder with lower density oil on top and water on the bottom.

In Vitro MRI Measurements. Images of the in vitro model were acquired on the same scanner using similar MRI anatomy and pcMR protocols to those used for the in vivo measurements previously described. During imaging, it was necessary to position the pump control and power supply far from the magnet so as to not risk causing damage to the scanner. Thus, the output of the pump system employed a ~7.6 meter section of nylon tubing (~6.1 mm OD, ~4.3 mm ID) before entering the flow model. The model was positioned in the center of the MRI scanning region. The length of tubing connecting the model was immobilized with tape so as to reduce flow variation caused by bulk movement of the tubing during operation.

Overall model geometry was scanned with a slice thickness of two millimeters over a length of 22 centimeters. Velocity measurements were conducted on the model with the syrinx open and closed to the atmospheric pressure (as previously explained in the in vitro model assembly). For each condition pcMR was used to acquire fluid velocity at three cross-sections through the model spaced 5 cm apart (Fig. 4). A single sagittal pcMR measurement was acquired so as to observe if any secondary flow patterns were present. Flow waveforms, geometry, and area changes were obtained in the same manner as described for the in vivo measurements. bSSFP cine MRI was used to obtain cross-sectional geometry changes during a cardiac cycle.

In Vitro Laboratory Measurements. The pressure inside and external to the syrinx was monitored within the in vitro model through use of internal and external pressure transducers (Fig. 4). The four external pressure sensors were diaphragm type transducers (Model DP15, Validyne, Northridge, CA). The length of tubing connecting the transducers to the model was minimized at less than 5 cm in order to be certain the resonance frequency of the transducers was above the frequency range of interest. Pressure inside the syrinx was measured through the use of four piezoelectric pressure tip catheters (Model SPR-835, Millar Instruments, Houston, TX). These catheters were chosen primarily due to their small size, so as to minimally disrupt the flow in the syrinx region. Phase difference between the diaphragm transducers and pressure tip catheters was determined to be nearly zero within the frequencies of interest (0–40 Hz).

In order to reduce error due to voltage drift, a calibration was performed before and after each experiment by measuring the voltage from each sensor at a low and high static pressure by varying the water height at the flow model outlet region. Sensitivity was individually computed before and after the experiment and then averaged to produce a mean sensitivity during the experiment.

Noise was present in the signals from the tip pressure catheters placed inside the syrinx. This was due to the fact that they are designed to measure pressure fluctuations during the cardiac cycle in the human body, whereas the pressure fluctuation in the syrinx model was relatively small (~6 mm Hg). The signal-to-noise ratio for the tip pressure catheters varied from 1.4 to 3.3 when measured at a mean pressure of 1 mm Hg. The noise was predominantly centered at 60 Hz making it necessary to apply a 40-Hz low pass filter after acquisition in order to interpret the data. Signal to noise ratio of the diaphragm transducers was approximately 10. Linearity coefficients of the tip catheters and diaphragm transducers measured over a range from 0 to 20 mm Hg were 0.95 and 0.98, respectively.

In vitro spinal cord wall motion was measured through use of a

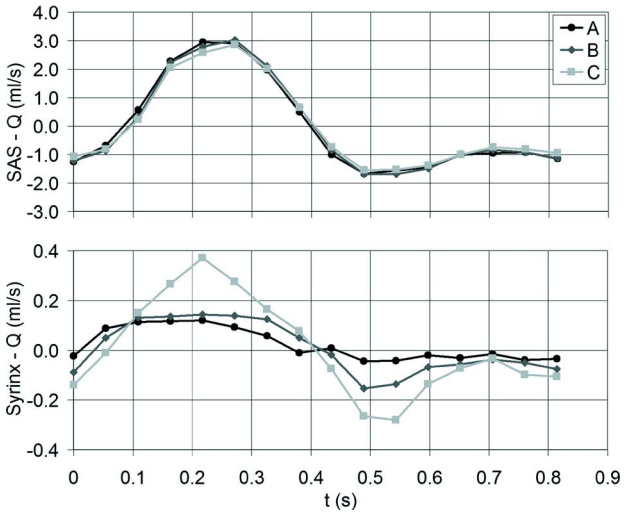

Fig. 5 In vitro model flow waveforms measured by pcMRI in the SAS (top) and syrinx (bottom) at positions A, B, and C on the model (measured with system open to the atmospheric pressure)

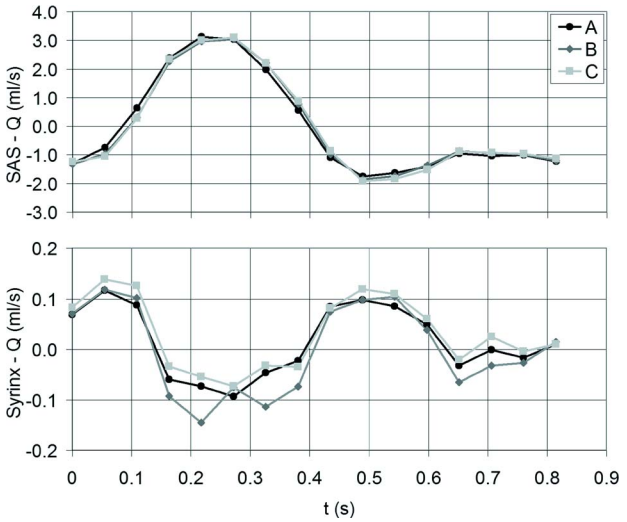

Fig. 6 In vitro model flow waveforms measured by pcMRI in the SAS (top) and syrinx (bottom) at position A, B, and C on the model (measured with system closed to the atmospheric pressure)

noncontacting laser Doppler vibrometer (LDV) (PDV 100, Polytec Inc., Tustin CA). The LDV enabled the measurement of wall velocity with μm/s precision. Figure 4 indicates the position of the reflective tape measurement points that were placed on the external surface of the syrinx wall in order to obtain the wall velocity. Each point was monitored individually while acquiring the input flow waveform to the pulsatile pump and pressure external and internal to the syrinx. A total of eighteen measurement points were spaced at 1-cm intervals along the length of the model at three polar locations approximately 90 deg from one another, referred to as "left," "top," and "right" (left, top, and right locations depicted in Fig. 3 cross-sectional view). It was not possible to obtain spinal cord wall motion on the "bottom" because this side of the model was covered by the external pressure transducers.

A 16-channel data acquisition card (Model DAQCard-6062E, National Instruments, Austin, TX) and break out box (Model BNC-2090, National Instruments) were used to obtain data sampled at 1 kHz for 16 860-ms pump cycles. The data was post-processed in computer software (MATLAB 12.0, Mathworks). Wall displacement was obtained by integrating the syrinx wall velocity measured by LDV. It was observed that during the acquisition period there was a mean positive offset voltage originating from the LDV signal causing the integrated displacement to have a linear increasing trend. This trend was removed from the data using the "linear" *detrend* command in MATLAB. To remove slight displacement variation from cycle to cycle, the displacement and pressure was computed from the ensemble average of 15 cycles aligned by the input flow waveform signal.

Results

Effects of the Syrinx Being Open or Closed. In vitro MRI measurements were taken on the model when the syrinx was open to the atmospheric pressure and closed to the atmospheric pressure as shown in Figs. 5 and 6, respectively. When the syrinx was closed to atmospheric pressure, the syrinx flow waveform was out of phase with the SAS flow waveform (Fig. 6) which is opposite to that observed in vivo (Fig. 7). Thus, it was resolved that pressure and vibration testing as well as detailed MRI data processing would be conducted only with the syrinx open to the atmospheric pressure.

MRI Measurements. Peak SAS flow in the patient at T3 during systole and diastole was 3.3 and 2.1 ml/s, respectively. Similarly, peak SAS flow in the model at position C during systole and diastole was 2.9 and 1.5 ml/s, respectively (see Fig. 4 for test position locations). The in vitro flow waveforms in the SAS and syrinx with the model open to the atmospheric pressure matched the magnitude and overall shape of that observed in vivo as shown in Figs. 5 and 7. Peak syrinx flow in the patient at T3 during systole and diastole was 0.56 and 0.20 ml/s, respectively. Similarly, peak syrinx flow in the model at C7 during systole and diastole was 0.37 and 0.28 ml/s, respectively. A summary of in vivo and in vitro flow peak-to-peak amplitudes is shown in Table 1. Some differences were observed during acceleration of the SAS flow waveforms. Velocity profile for flow in the SAS of the in

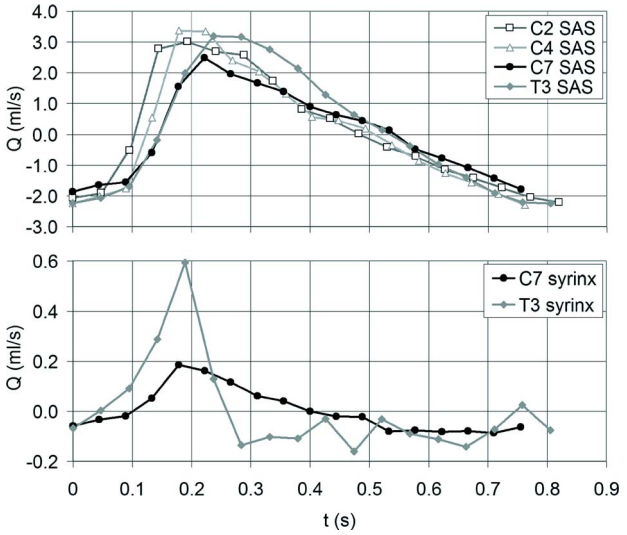

Fig. 7 In vivo patient flow waveforms measured by pcMRI in the SAS (top) and syrinx (bottom) at various vertebrae locations

Table 1 Comparison of flow peak-to-peak amplitude in the SAS and syrinx for the in vivo and in vitro experiments

In vivo ΔQ peak-to-peak amplitude (ml/s)			In vitro ΔQ peak-to-peak amplitude (ml/s)		
Axial Position (mm)	SAS	Syrinx	Axial Position (mm)	SAS	Syrinx
C2	5.2		A	4.6	0.2
C4	5.7		B	4.7	0.3
C7	4.3	0.3	C	4.4	0.7
T3	5.4	0.8			
AVG	5.2	0.5	AVG	4.6	0.4
σ	0.6	0.3	σ	0.2	0.3

vitro model is depicted in Fig. 8. Note that mean velocity in the SAS and syrinx was higher in vivo than in vitro since the cross-sectional area was less in the patient.

Wetted perimeter and cross-sectional area in the syrinx region were computed at each axial cross-section for both the in vivo and in vitro MRI experiment. The resulting range of values was used to determine the average and standard deviation (average$\pm\sigma$) of various fluid dynamics parameters shown in Table 2. The peak Re and Womersley numbers were computed for the SAS and syrinx both in vivo and in vitro. Peak Re numbers were less than 200 for all cases and thus insured the flow to be laminar throughout the cardiac cycle. Average and standard deviation of Womersley numbers in vivo for the SAS and syrinx (shown in Fig. 2) were 7.1 ± 1.5 and 9.4 ± 0.8, respectively. Average values of α were 9.1 ± 0.5 and 21 ± 0.3, respectively, for the in vitro model. Axial velocity profiles are shown at different points during the cardiac cycle for both the in vitro model and in vivo (Figs. 9 and 10). In addition, secondary flow patterns were examined in the sagittal plane through pcMR measurement and found to be negligible in comparison to the axial velocity.

MRI measurement for changes in the cross-sectional area during the cardiac cycle for the in vitro model obtained using bSSFP cine MRI did not show a trend related to the cardiac cycle and appeared have significant noise. However, changes in flow waveform between two axial locations were shown to be significant both in vivo and in vitro by plotting the difference in flows at two separate axial locations as shown in Fig. 11. Based on these flow differences, the maximum cross-sectional area change during the cardiac cycle was estimated to be 0.45 and 0.33 mm^2 for the in vivo and in vitro cases, respectively.

Table 3 indicates the measured spinal cord thickness at various

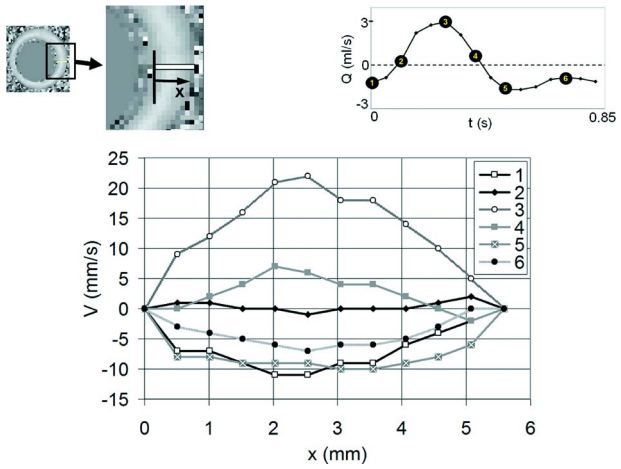

Fig. 8 In vitro velocity profiles measured by pcMRI in the SAS at various time points during the cardiac cycle (see flow waveform inset)

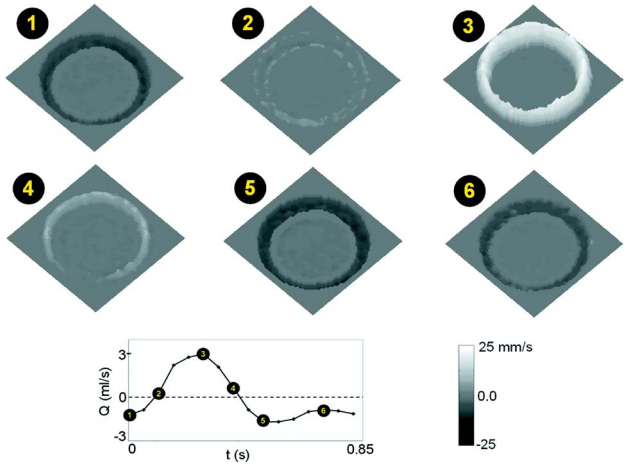

Fig. 9 In vitro velocity profile obtained from pcMRI at position B indicated at various time points during the cardiac cycle (see flow waveform inset)

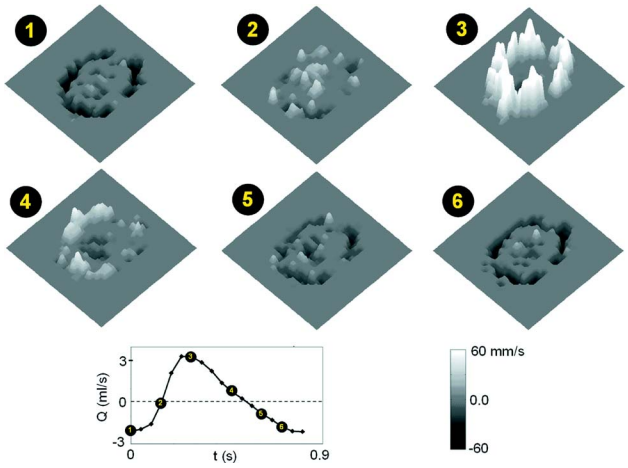

Fig. 10 In vivo patient velocity profile obtained from pcMRI measured at T3, indicated at various time points during the cardiac cycle (see flow waveform inset)

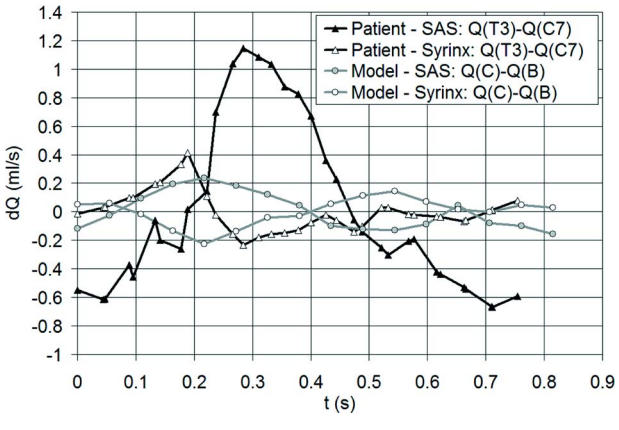

Fig. 11 Computed flow difference in the SAS and syrinx measured by pcMRI. Patient measurements between C7 and T3 cervical levels located 6 cm apart. Model measurements obtained between C and B locations, 5 cm apart.

Table 3 In vitro spinal cord thickness and wall displacement peak-to-peak amplitude (thickness (mm)/displacement (μm)) measured at 1, 7, 13, and 18 cm from the in vitro model flow inlet. P_{diff} indicates corresponding differential pressure amplitude at each axial location.

Axial Location	Left (mm/μm)	Top (mm/μm)	Right (mm/μm)	Bottom (mm)	P_{diff} (mm Hg)
1 cm	1.93/27	1.32/74	1.98/25	1.93	2.87
7 cm	2.00/52	1.32/144	1.88/38	2.21	2.09
13 cm	2.16/31	1.24/124	1.57/45	1.68	2.66
18 cm	2.11/28	1.50/94	1.57/17	2.00	2.36
AVG	2.01/35	1.34/120	1.65/34	1.91	2.50
σ	0.10/13	0.16/20	0.19/11	0.17	0.34

axial locations and angular positions as well as the displacement amplitude at each location. Thickness measurements were obtained after dissecting the model and measuring it at each location with a micrometer. The displacement of the bottom side of the model is not indicated because it was not possible to measure due to obstruction by the pressure transducers. The P_{diff} column quantifies the differential pressure amplitude at each axial location. The measurements generally indicate that where the wall is thinner the motion is larger and vice versa. However, further experiments are required to fully understand the relationship of wall movement and thickness.

In Vitro Pressure Measurement. Figure 12 indicates the internal syrinx, external SAS, and differential (internal−external) pressure measurements taken at four axial locations along the model. The computed differential pressure shown on the bottom portion of Fig. 12 indicates that the mean pressure in the syrinx is approximately 0.5 mm Hg greater than the SAS, which is similar to in vivo pressure gradients previously reported in the literature [23].

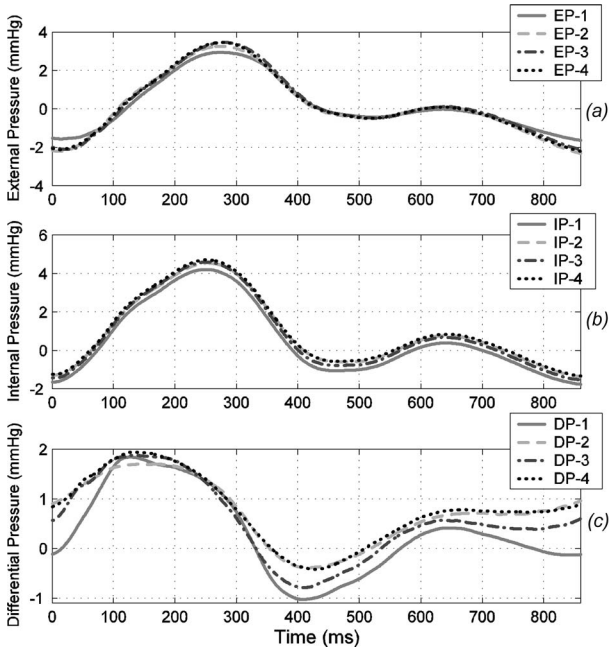

Fig. 12 In vitro pressure versus time measured at four axial locations. (*a*) external pressure (EP), (*b*) internal pressure (IP), (*c*) differential pressure (DP). Measurement 1, 2, 3, and 4 correspond to location 1, 7, 13 and 17 cm on the model as shown in experimental configuration (Fig. 4).

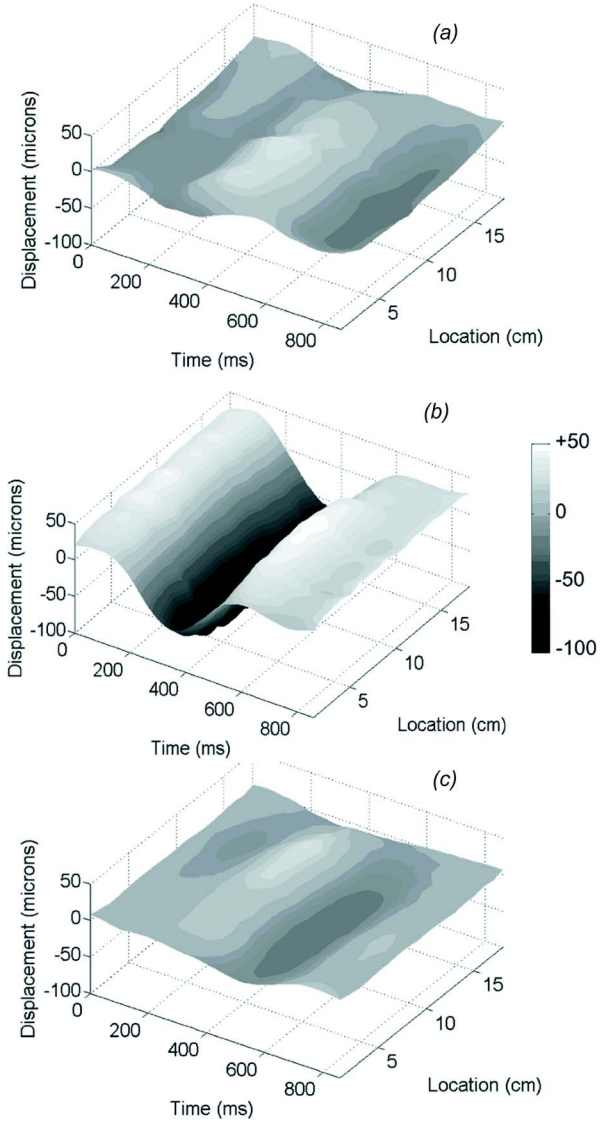

Fig. 13 Ensemble average radial wall displacement as a function of axial location for one cardiac cycle (*a*) = left wall; (*b*) = top wall; (*c*) = right wall, location of left, top, and right wall depicted in Fig. 3 cross-sectional view

It is apparent that during ~200 ms of the 860-ms flow pump cycle the syrinx pressure is less than the external SAS pressure.

In Vitro Spinal Cord Wall Movement. Figure 13 is a summary of the vibration results obtained from LDV testing. Each section of the figure indicates the displacement of a line of LDV test points taken at a single polar location ("left," "top," "right"). Figure 13 shows that the amplitude and phase relation of wall motion varies for the same axial location depending on what polar position the measurements are taken from (i.e., nonaxisymmetric). The relation of wall motion and differential pressure for the four test locations is shown in Fig. 14. The phase relation of pressure and wall motion varies depending on the polar location of wall motion measurement. In order to determine that the phase difference was not present due to instability of the system caused by low internal pressure loading in the syrinx, the experiment was conducted at elevated internal syrinx pressure of 20 cm water. This experiment resulted in the same overall trend of phase and magnitude relation in wall movement as shown in Fig. 15. However, wall motion magnitude was reduced approximately by a factor of 2.

In order to quantify bulk motion of the entire model, an LDV

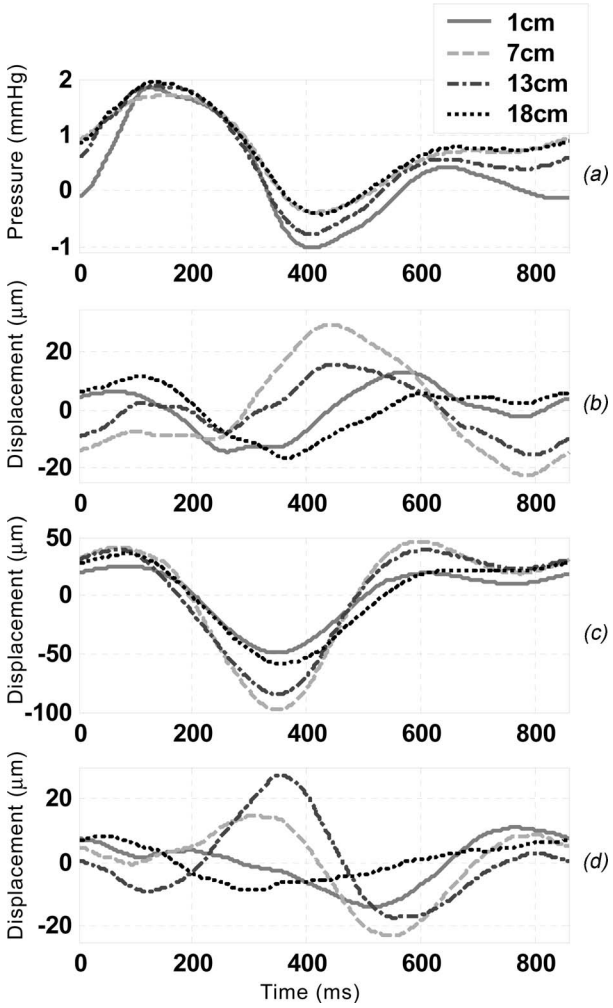

Fig. 14 In vitro differential pressure and wall displacement measurements. (*a*) Differential pressure (internal–external measured at four axial locations. (*b*) Left wall displacement measured at four axial locations. (*c*) Top wall displacement measured at four axial locations. (*d*) Right wall displacement measured at four axial locations.

measurement point on the external surface of the model was monitored and compared to the movement obtained from a nearby measurement point on the spinal cord wall near the end pin. Measurements were taken at one axial location on all three sides of the model. The data indicated that the bulk motion of the model was in phase with the input flow waveform and a maximum of 10 μm peak to peak, whereas the minimum peak-to-peak motion of the syrinx wall was approximately 30 μm, with a maximum of 140 μm. This indicates that bulk motion of the model was small in comparison to the spinal cord wall motion.

Discussion

The results presented describe the hydrodynamics of syringomyelia both in vivo and in vitro. First, the similarities and differences of the in vivo and in vitro geometry as well as hydrodynamics are described. Emphasis is placed on direct comparison of results so as to determine what extent the in vitro model reproduces the pathological in vivo hydrodynamics. Second, the complex interaction between flow, pressure, and spinal cord wall movement and their importance in syrinx pathogenesis is discussed.

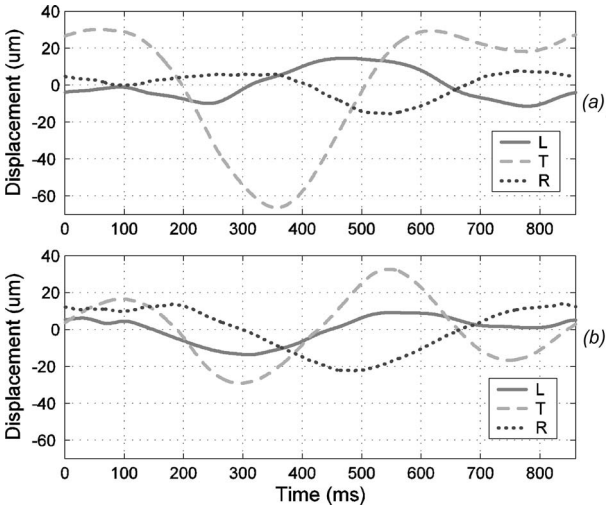

Fig. 15 In vitro wall displacement measured with low and elevated internal syrinx pressure. (*a*) Low mean internal syrinx pressure (~1 cm H_2O). (*b*) Elevated mean internal syrinx pressure (~20 cm H_2O).

Geometry. The in vitro spinal cord was not axisymmetric having thickness variation from 1.75 to 0.58 mm depending on the angular position and axial location (Table 3). However, considering the presence of nerve roots and blood vessels as well as axial variation in syrinx diameter in vivo, it can be concluded that the in vitro model is far more symmetric than the in vivo case. The in vitro model did not have any curvature, whereas curvature is present in vivo. Loth et al. note that significant Dean flow patterns can result when CSF travels from the SAS in the brain into the spinal canal region if curvature is significant [1].

Syrinx Cross Sectional Area Change. Using the volume change method, described in the in vivo MRI methods section, the maximum axially averaged cross-sectional area change over 5 cm during the cardiac cycle was computed to be 0.45 and 0.33 mm^2 for the in vivo and in vitro cases, respectively. This area change is computed over a 5-cm length and does not detail wall motion differences axially or circumferentially. Note that small area change is probably not quantifiable using bSSFP cine MRI since the maximum area change is on the order of one pixel.

Open Versus Closed System. Flow versus time data in Figs. 5 and 6 indicate that a fundamental difference in flow results when the syrinx is open or closed to the atmospheric pressure. In the case when the syrinx is open, the internal and external fluid motions are in phase with one another. When the syrinx is closed, the syrinx flow occurs approximately 180 deg after the SAS flow. Since internal and external flow waveforms are in phase with one another in vivo [23], this result suggests that some mechanism exists in the syrinx to relieve pressure to the atmospheric pressure in vivo. Influence of atmospheric pressure on intracranial pressure in primates has been documented by Kiel in 1992 [34]. It can be concluded that the in vitro model better mimics in vivo flow when the syrinx is open to the atmospheric pressure.

Flow Amplitude and Velocity. Results indicate that the amplitude of flow in the SAS and syrinx of the model mimic the in vivo case in both magnitude and shape (Table 1 and Figs. 5 and 7). Variation in flow waveform shape is partly caused by compliance present in the nylon tubing that connected the syringe pump and flow model. Since the end conditions of the SAS are different

between the in vitro model and in vivo case, the resulting differences in pressure reflections may also contribute to variations in flow waveform shape. In addition, the velocities do not match, with greater velocity in vivo than in vitro due to differences in cross-sectional area (Figs. 9 and 10). It was also observed that in vivo and in vitro flow amplitude increased for each axial measurement location moving caudally away from the brain (Figs. 5 and 7). The reason for caudal increase in flow amplitude is not examined in detail here, but may be due to the complex fluid structure interaction of the CSF and spinal cord wall. Note that flow amplitude did not increase caudally for in vitro tests conducted with the system closed to the atmospheric pressure (Fig. 6). Reynolds and Womersley numbers are similar but can be different by as much as a factor of 2. The large diameter of the in vitro syrinx was selected in order to examine the worst case scenario of syringomyelia. This large diameter geometry was observed in another syringomyelia patient in which detailed flow information was not available.

Velocity Profile. The velocity profiles measured in vivo and in vitro agree macroscopically at various time points during the cardiac cycle (Figs. 9 and 10). However, the in vivo measurements have significant noise and thus are difficult to compare quantitatively. The SAS profiles in vitro appear to be similar to that of a classic Womersley flow with large Womersley numbers ($\sim$9.0), giving rise to inertial dominated flow with blunt profiles. In some cases "M" shaped profiles within the SAS can be observed during systolic acceleration (time point 2, Figs. 8 and 9). It is not possible to detect profiles within the syrinx due to the low velocities. Since Womersley numbers within the syrinx are high ($>$9), we expect the syrinx to have fairly blunt Womersley-like profiles.

Spinal Cord Wall Motion. Detailed measurements of spinal cord wall dynamics have not been quantified in vivo except for intraoperative ultrasound [23], which alters the true in vivo pressure environment. While area changes cannot be quantified by LDV, these measurements were able to capture the spinal cord motion and, to some extent, cross-sectional shape variation during the cardiac cycle. The in vitro model presents otherwise unobtainable details about the pressure and syrinx wall dynamics. The spinal cord wall motion results depicted in Fig. 13 indicate the wall motion at each of the three polar positions as a function of time. Although only three polar locations were observed, the data is sufficient evidence to conclude that the wall motion is nonaxisymmetric. Nonaxisymmetric spinal cord wall motion is an important observation and would be expected to be present in vivo since asymmetry is likely greater. Nonaxisymmetric spinal cord wall motion is not accounted for in the syringomyelia hydrodynamic analysis by Carpenter and co-workers [12,17].

Wave Transmission. The speed of the wall motion wave is visible to some extent in Fig. 13, but not possible to accurately quantify. The wave transmission can be best observed in the data from the "right" side of the model. The main wall movement, "top," follows intuition in that when the pressure differential is negative, the wall moves inward and likewise, when the pressure differential is positive, the wall moves outward. The pressure differential appears to lead the wall motion by approximately 50 ms (Fig. 15). A parameter of interest is the pulse wave velocity (PWV) within the SAS and syrinx as it is an indicator of the speed pressure waves are transmitted as well as the inherent system compliance. While a precise value is not measurable with this experimental setup, one can estimate the lower range to be $\sim$20 m/s when a 10-ms pressure signal phase delay is approximated from Fig. 12. PWV can be computed for a straight flexible pipe using the Moen-Korteweg equation ($c^2=hE/D\rho$, c is PWV, h is wall thickness, E is Young's modulus, D is tube diameter, ρ is fluid density). However, this equation is not applicable to the coaxial tube system because it is based on shell theory, which assumes that the structure of interest supports bending moments. The compliant hollow spinal cord system can likely be better examined through analysis

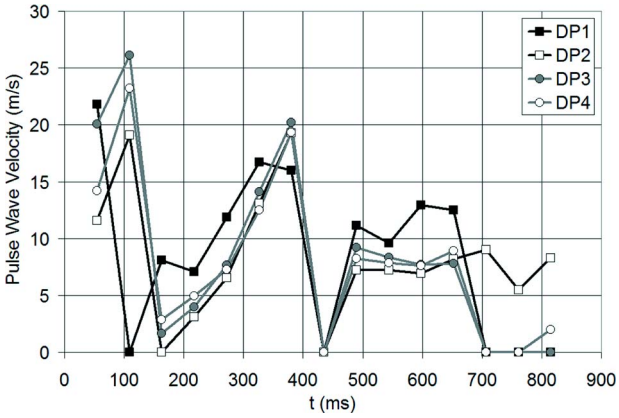

Fig. 16 Variation of pulse wave velocity during the cardiac cycle for the in vitro model as estimated through the Moen-Korteweg equation. Note that zero values indicate the algebraic expression produced an imaginary value for pulse wave velocity.

based on membrane theory, which does not support bending moments. A more relevant method to compute the PWV in the coaxial tube system involves the use of a different form of the Moen-Korteweg equation ($c^2=(A/\rho)[(dP/dt)/(dA/dt)]$). In this form of the equation, dP/dt is computed using the difference in pressure, $P(t)$ (syrinx-SAS). The area change as a function of time $[\Delta A(t)]$ was obtained through the volume change method previously described and used to determine dA/dt. A first-order backward difference method was used to obtain the derivative of the flow difference measured by pcMR between positions B and A as well as B and C of the model as shown in Fig. 16. A maximum PWV of $\sim$25 m/s was computed using the method described. Intermediate values of PWV during the cardiac cycle were found to be similar to those previously observed by Williams (13.5 m/s), Carpenter et al. (2.2–4 m/s), and Greitz et al. (4 m/s) [6,12,15]. To our knowledge, time variation of PWV in the syrinx has not been reported in the literature.

Syrinx and SAS Pressure. Figure 12 indicates the syrinx pressure, SAS pressure, and differential pressure (syrinx-SAS) measured from the four internal and external pressure transducers as indicated in Fig. 4. Pressure peak-to-peak amplitude inside and external to the syrinx (4 mm Hg) was greater than the in vivo measurements reported in the literature (1 mm Hg) [23]. The in vitro mean pressure measured in the SAS was lower than the syrinx by approximately 0.5 mm Hg, causing a driving force for fluid movement out of the syrinx. In Fig. 12, the internal pressure in the syrinx is less than the external pressure for approximately 200 ms during each 860-ms flow cycle. The transient negative pressure differential is a mechanical force that could cause transfer of fluid from the SAS to the syrinx. This measurement has not been reported in the literature [24]. It can be hypothesized that variation in the external SAS waveform could cause the negative pressure differential to increase in amplitude as well as length. A number of sources exist that can cause variation in the SAS pressure including, coughing and sudden posture changes. It has been hypothesized that transient pressure variation caused by these conditions could be a source of syrinx pathogenesis [24,35]. The negative pressure differential is likely due to the inertia of the fluid wall interaction in the unsteady system. Given the pressure differential results, one scenario that could lead to the development of a syrinx is a one-way fluid valve, which prefers fluid moving into the syrinx rather than out. Note that the internal syrinx pressure wave leads the external SAS pressure wave by approximately 40 ms (Fig. 15).

Damping Factor and Fundamental Resonant Frequency. To de-

termine the in vitro model damping factor and fundamental resonant frequency, a short test was conducted which consisted of applying a sudden flow input to the model while monitoring external SAS pressure with a transducer. The damping ratio (δ) and damping factor (ξ) were calculated using the log-decrement method $[\delta=\ln(x_1/x_2), \xi=\delta/(4\pi^2+\delta^2)]$ and found to be $\sim 0.9 \pm 0.15$, and 0.14, respectively. The system fundamental resonant oscillations were determined to be ~ 8.4 Hz which is similar to the 5-Hz resonance recorded through cisternal puncture during patient coughing by Williams [6]. Intrathecal pressure fluctuation during coughing has been recorded by Sansur et al., but a resonant frequency cannot be quantified through the plots provided [36]. Based on the agreement between resonant oscillations, it is tempting to assume that in vitro and in vivo compliance are similar. However, it is not possible to conclude since the fluid structure system resonance is dependant on many factors including geometry, which is shorter in vitro than in vivo.

Syrinx Size Reduction, Elimination, or Stabilization. Observation of elevated mean pressure in the syrinx and lower pressure in the SAS, along with the phase difference between the two pressure waves, describes the essential hydrodynamic environment which hinders the regression of the syrinx cavity. Three possible means of reducing the negative SAS-syrinx pressure differential, that may reduce fluid accumulation in the syrinx, are discussed. The desired patient outcome is syrinx size reduction, elimination or stabilization. The first, and most intuitive, mechanical means to force fluid out of the syrinx, is to increase syrinx pressure. This could be accomplished by squeezing the syrinx wall or by filling the syrinx with more fluid, of which both are not reasonable solutions since this might lead to an increase in syrinx size or rupture. The second is to decrease the SAS pressure. This could be accomplished through draining CSF, which is done clinically, or by increasing the compliance of the spinal compartment. Draining CSF from the SAS only provides a temporary solution since the body constantly replenishes it. Increasing the compliance of the spinal compartment is difficult since it requires surgical intervention such as decompression surgery. In addition, while this may reduce SAS pressure, it will likely reduce syrinx pressure by a similar amount. A third possible solution is to eliminate or reduce the phase difference of the syrinx and SAS pressure waves by either slowing the syrinx wave or speeding up the SAS wave. Speeding up the syrinx pressure wave would require stiffening of the syrinx wall, which is difficult to accomplish. A more plausible solution is to increase the speed of transmission of the SAS pressure wave. This can be accomplished through an increase in the SAS cross-sectional area. However, it has been observed that even when the fluid is unobstructed, as in the in vitro study, a transient negative pressure differential can exist. This result may support why the traditional solution of removing obstruction to CSF flow in the hindbrain does not always result in reduction of syrinx size.

Conclusions

A phantom model that approximates in vivo syringomyelia hydrodynamics in a single patient has been described. In vivo and in vitro syrinx area change has been quantified to be small but measurable. Spinal cord wall motion, that is otherwise unobtainable through use of MRI, was observed in vitro and shown to be nonaxisymmetric. Although, assumptions of axisymmetric wall motion of the spinal cord help simplify the complex system, such assumptions probably do not accurately portray the in vivo environment. Transient negative pressure differential has been recorded and could provide a means for syrinx development. PVW within the syrinx varies during the cardiac cycle and was computed to be a maximum of 25 m/s. Future testing is necessary to determine the importance of CSF flow waveform variations due to the effects of flow obstruction (Chiari I malformation, vertebrae misalignment), breathing, coughing, and hydrocephalus. Studies with in vitro models of this type may provide better understanding of the importance of hydrodynamics on syrinx formation, progression, and regression after decompression surgery.

Acknowledgments

The authors give special thanks to the American Syringomyelia Alliance Project, The Labuda Family Foundation, and Motorola Inc., which have been responsible for funding this research. The authors also thank Tom Kotsakos for material property testing, Todd Spohnholtz for help in data acquisition methods, and David Smith for help in interpretation of the results. In addition, Wojciech Kalata would like to express deep appreciation to the American Council for Polish Culture for Brigadier General Casimir Pulaski Scholarship for Advanced Studies.

References

[1] Loth, F., Yardimci, M. A., and Alperin, N., 2001, "Hydrodynamic Modeling of Cerebrospinal Fluid Motion within the Spinal Cavity," ASME J. Biomech. Eng., **123**(1), pp. 71–79.
[2] Soderbergh, S., et al., *Gray's Anatomy*, 1997, Fox Lorber Home Video, New York, NY, 1 videocassette (80 min.).
[3] Bradbury, M. W. B., *The Concept of a Blood-brain Barrier*, 1979, Wiley, Chichester, NY, p. 465.
[4] Davson, H., *Physiology of the Cerebrospinal Fluid*, 1967, Little Brown, Boston, Vol. VII, p. 445.
[5] Dunbar, H. S., Guthrie, T. C., and Karpell, B., 1966, "A Study of the Cerebrospinal Fluid Pulse Wave," Arch. Neurol., **14**(6), pp. 624–630.
[6] Williams, B., 1976, "Cerebrospinal Fluid Pressure Changes in Response to Coughing," Brain, **99**(2), pp. 331–346.
[7] Bloomfield, I. G., Johnston, I. H., and Bilston, L. E., 1998, "Effects of Proteins, Blood Cells and Glucose on the Viscosity of Cerebrospinal Fluid," Pediatr. Neurosurg., **28**(5), pp. 246–251.
[8] Uftring, S. J., et al., 2000, "The Mechanical State of Intracranial Tissues in Elderly Subjects Studied by Imaging CSF and Brain Pulsations," Magn. Reson. Imaging, **18**(8), pp. 991–996.
[9] Klekamp, J., 2002, "The Pathophysiology of Syringomyelia—Historical Overview and Current Concept," Acta Neurochir., **144**(7), pp. 649–664.
[10] Gardner, W. J., 1965, "Hydrodynamic Mechanism of Syringomyelia: Its Relationship to Myelocele," J. Neurol., Neurosurg. Psychiatry, **28**, pp. 247–259.
[11] Williams, B., 1969, "The Distending Force in the Production of Communicating Syringomyelia," Lancet, **2**(7622), p. 696.
[12] Carpenter, P. W., Berkouk, K., and Lucey, A. D., 2003, "Pressure Wave Propagation in Fluid-filled Co-axial Elastic Tubes. Part 2: Mechanisms for the Pathogenesis of Syringomyelia," ASME J. Biomech. Eng., **125**(6), pp. 857–863.
[13] Ball, M. J., and Dayan, A. D., 1972, "Pathogenesis of Syringomyelia," Lancet, **2**(7781), pp. 799–801.
[14] Oldfield, E. H., et al., 1994, "Pathophysiology of Syringomyelia Associated with Chiari I Malformation of the Cerebellar Tonsils. Implications for Diagnosis and Treatment," J. Neurosurg., **80**(1), pp. 3–15.
[15] Greitz, D., Ericson, K., and Flodmark, O., 1999, "Pathogenesis and Mechanics of Sprinal Cord Cyst. A New Hypothesis Based on Magnetic Resonance Studies of Cerbrospinal Fluid Dynamics," J. Neuroradiol., **5**(2), pp. 61–78.
[16] Greitz, D., et al., 1994, "MR Imaging of Cerebrospinal Fluid Dynamics in Health and Disease. On the Vascular Pathogenesis of Communicating Hydrocephalus and Benign Intracranial Hypertension," Acta Radiol., **35**(3), pp. 204–211.
[17] Berkouk, K., Carpenter, P. W., and Lucey, A. D., 2003, "Pressure Wave Propagation in Fluid-filled Co-axial Elastic Tubes. Part 1: Basic Theory," ASME J. Biomech. Eng., **125**(6), pp. 852–856.
[18] Amabili, M., Pellicano, F., and Paidoussis, M. A., 2001, "Nonlinear Stability of Circular Cylindrical Shells in Annular and Unbounded Axial Flow," ASME J. Appl. Mech., **68**(6), pp. 827–834.
[19] Cirovic, S., Walsh, C., and Fraser, W. D., 2002, "Wave Propagation in a System of Coaxial Tubes Filled with Incompressible Media: A Model of Pulse Transmission in the Intracranial Arteries," J. Fluids Struct., **16**(8), pp. 1029–1049.
[20] Mazuch, T., 2001, "Approximate Modelling of Fluid Influence on Axisymmetric Wave Dispersion in an Infinite Hollow Cylinder," J. Sound Vib., **245**(4), pp. 611–631.
[21] Paidoussis, M. P., Mateescu, D., and Sim, W. G., 1990, "Dynamics and Stability of a Flexible Cylinder in a Narrow Coaxial Cylindrical Duct Subjected to Annular-Flow," ASME J. Appl. Mech., **57**(1), pp. 232–240.
[22] Pellicano, F., Amabili, M., and Vakakis, A. F., 2000, "Nonlinear Vibrations and Multiple Resonances of Fluid-filled, Circular Shells. Part 2: Perturbation Analysis," ASME J. Vibr. Acoust., **122**(4), pp. 355–364.
[23] Heiss, J. D., et al., 1999, "Elucidating the Pathophysiology of Syringomyelia," J. Neurosurg., **91**(4), pp. 553–562.
[24] Levine, D. N., 2004, "The Pathogenesis of Syringomyelia Associated with Lesions at the Foramen Magnum: A Critical Review of Existing Theories and Proposal of a New Hypothesis," J. Neurol. Sci., **220**(1-2), pp. 3–21.
[25] Loth, F., et al., 1997, "Measurements of Velocity and Wall Shear Stress Inside a PTFE Vascular Graft Model Under Steady Flow Conditions," ASME J. Bio-

mech. Eng., **119**(2), pp. 187–194.
[26] Lei, M., et al., 2001, "Pulsatile Flow in an End-to-side Vascular Graft Model: Comparison of Computations with Experimental Data," ASME J. Biomech. Eng., **123**(1), pp. 80–87.
[27] Kalata, W., 2002, "Numerical Simulation of Cerebrospinal Fluid Motion Within the Spinal Canal," Masters thesis, University of Illinois at Chicago, Chicago.
[28] Yedavalli, R. V., et al., 2001, "Construction of a Physical Model of the Human Carotid Artery Based Upon In Vivo Magnetic Resonance Images," ASME J. Biomech. Eng., **123**(4), pp. 372–376.
[29] Silver, F. H., 1987, *Biological Materials: Structure, Mechanical Properties, and Modeling of Soft Tissues*. New York University Biomedical Engineering Series. New York University Press, New York, Vol. xx, p. 228.
[30] Fung, Y. C., 1981, *Biomechanics: Mechanical Properties of Living Tissues*," Springer-Verlag, New York, Vol. xii, p. 433.
[31] Yamada, H., and Evans, F. G., 1970, *Strength of Biological Materials*, Williams & Wilkins, Baltimore, Vol. x, p. 297.
[32] Elden, H. R., 1971, *Biophysical Properties of the Skin*, Wiley-Interscience, New York, Vol. viii, p. 645.
[33] Schmid, H., and Michel, B., 2000, "Siloxane Polymers for High-resolution, High-accuracy Soft Lithography," Macromolecules, **33**(8), pp. 3042–3049.
[34] Keil, L. C., et al., 1992, "The Effect of Head-down Tilt and Water Immersion on Intracranial Pressure in Nonhuman Primates," Aviat., Space Environ. Med., **63**(3), pp. 181–185.
[35] Bertrand, G., 1973, "Chapter 26. Dynamic Factors in the Evolution of Syringomyelia and Syringobulbia," Clin. Neurosurg., **20**, pp. 322–333.
[36] Sansur, C. A., et al., 2003, "Pathophysiology of Headache Associated with Cough in Patients with Chiari I Malformation," J. Neurosurg., **98**(3), pp. 453–458.